Editors' Suggestion

Mechanical control of crystal symmetry and superconductivity in Weyl semimetal $MoTe_2$

Colin Heikes,[1] I-Lin Liu,[1,2,3] Tristin Metz,[2] Chris Eckberg,[2] Paul Neves,[1,2] Yan Wu,[4] Linda Hung,[1] Phil Piccoli,[5] Huibo Cao,[4] Juscelino Leao,[1] Johnpierre Paglione,[2] Taner Yildirim,[1] Nicholas P. Butch,[1,2] and William Ratcliff II[1,*]

[1]*NIST Center for Neutron Research, NIST, Gaithersburg, Maryland 20899, USA*

[2]*Center for Nanophysics and Advanced Materials, University of Maryland, College Park, Maryland 20742, USA*

[3]*Department of Materials Science and Engineering, University of Maryland, College Park, Maryland 20742, USA*

[4]*Neutron Scattering Division, Oak Ridge National Laboratory (ORNL), Oak Ridge, Tennessee 37831, USA*

[5]*Department of Geology, University of Maryland, College Park, Maryland 20742, USA*

(Received 24 April 2018; published 30 July 2018)

The noncentrosymmetric Weyl semimetal candidate $MoTe_2$ was investigated through neutron-diffraction and transport measurements at pressures up to 1.5 GPa and at temperatures down to 40 mK. Centrosymmetric and noncentrosymmetric structural phases were found to coexist in the superconducting state. Density functional theory (DFT) calculations reveal that the strength of the electron-phonon coupling is similar for both crystal structures. Furthermore, it was found that by controlling nonhydrostatic components of stress, it is possible to mechanically control the ground-state crystal structure. This allows for the tuning of crystal symmetry in the superconducting phase from centrosymmetric to noncentrosymmetric. DFT calculations support this strain control of crystal structure. This mechanical control of crystal symmetry gives a route to tuning the band topology of $MoTe_2$ and possibly the topology of the superconducting state.

DOI: 10.1103/PhysRevMaterials.2.074202

Topological superconductivity, which arises when a bulk superconducting state coexists with a topologically nontrivial band structure, leading to gapless surface states in a superconducting system, is of particular interest and excitement due to the possibility of stabilizing exotic Majorana excitations [1]. One promising route to realizing topological superconductivity is finding superconductivity in materials with topologically nontrivial band structures, as is found in semimetallic $MoTe_2$, where both superconductivity and a type-II Weyl semimetallic state have been reported [2–8]. This type-II Weyl semimetallic state is enabled by an inversion symmetry-breaking structural transition which takes place at a transition temperature (T_S) around 250 K [9–11]. The superconductivity, topology, and structure of $MoTe_2$ have been demonstrated to be strongly influenced by both doping [8,11–17] and pressure [2,4,11]. Interestingly, pressure and doping increase the superconducting transition temperature (T_c) while apparently reducing T_S, though the coupling between the electronic ground state and the crystal structure is an open question. Here we study the effect of pressure on both superconductivity and the observed structural phase transition in detail and show that the deliberate application of pressure in hydrostatic or nonhydrostatic form allows us to control the crystal symmetry in this material and thus gives us a route to tuning the topology of the superconducting state.

The proposed type-II Weyl semimetal and superconductor $MoTe_2$ offers the opportunity for realizing topological superconductivity through the coexistence of a topologically nontrivial band structure with superconductivity. An open question in this material is the nature of the interplay between pressure, the electronic ground state, and the structural transition between a centrosymmetric monoclinic structure (the $1T'$ phase) and a noncentrosymmetric orthorhombic structure (the T_d phase). We show through a combination of temperature- and pressure-dependent transport and elastic neutron-scattering measurements that the two possible structures can coexist at a range of pressures and temperatures concurrent with superconductivity. We also illustrate that the ground-state crystal structure can be controlled independently of the superconductivity, through nonhydrostatic stress, allowing for a centrosymmetric superconducting state, a noncentrosymmetric superconducting state, or a superconducting mixed structure state. Our density functional theory (DFT) calculations illustrate the near degeneracy of the two structural phases as well as the small energy barrier between phases, explaining our observation of a mixed phase state under hydrostatic pressure conditions. Unlike the typical case of inversion symmetry-breaking structural transitions in perovskite ferroelectrics or geometrically designed polar metals [18,19], we also show that this structural transition is driven not by a phonon mode softening to an imaginary vibrational frequency as is suggested in [20], but rather by entropic considerations. Our calculations illustrate that the pressure-dependent superconductivity in $MoTe_2$ can be reproduced from single layer simulations, consistent with the decoupling of crystal structure and superconductivity. Further, our calculations offer justification for why nonhydrostatic stresses alter the ground-state crystal structure and allow for selection between centrosymmetric and noncentrosymmetric states.

We have performed temperature-dependent longitudinal resistivity measurements as well as longitudinal magnetoresistance measurements on a variety of crystals from multiple batches as described in the Supplemental Material [21]. The

*Corresponding author: william.ratcliff@nist.gov

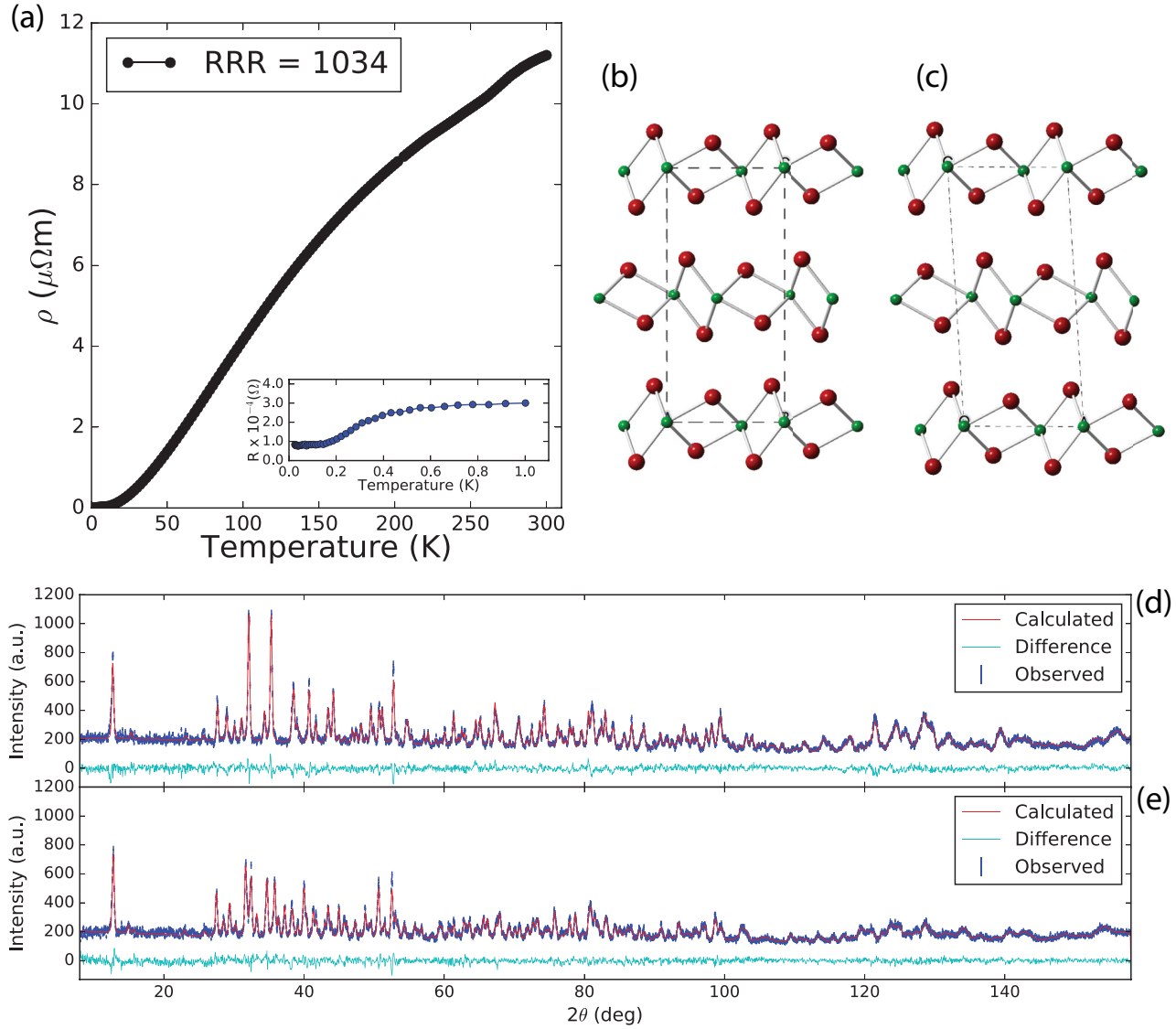

FIG. 1. Structure and transport of $MoTe_2$ single crystals. (a) Temperature-dependent longitudinal resistivity of a single crystal with a RRR value of 1034 typical of our synthesis. The inset illustrates the second turnover and nonzero saturation of the resistivity below 1 K indicative of the onset of incomplete superconductivity. (b), (c) Crystal structure of the T_d (b) and $1T'$ (c) phases of $MoTe_2$ illustrating the shear displacement of the unit cell. (d), (e) Reitveld refined neutron powder-diffraction measurements of $MoTe_2$ at 3 K in the T_d phase (d) and at 300 K in the $1T'$ phase (e). Powder fit parameters and refinement statistics are shown in Tables S1–S3 in the Supplemental Material [21].

results for a typical crystal are shown in Fig. 1(a). We clearly see the transport anomaly associated with the structural transition (at T_S) from the monoclinic $1T'$ phase to the T_d phase [2,8,22,23]. This particular crystal shows a RRR value (defined as the ratio of the resistance at 300 K to the resistance at 2 K) of >1000 as well as a MR ratio of $>190\,000\%$ at 2 K and 15 T which illustrates the high sample quality. From electron probe microanalysis/wavelength-dispersive x-ray spectroscopy (EPMA-WDX), we measure that our crystals have stoichiometric composition within our measurement error, with no obvious trends in residual resistivity ratio (RRR) value with sample composition and no apparent composition gradients within a given crystal. As is shown in the inset of Fig. 1(a), this sample also has a resistive turnover above a temperature of 0.4 K indicating the onset of superconductivity (T_c), which is consistent with the sample quality dependent superconductivity reported in [8]. However, we do not see a full transition to a zero resistance state at ambient pressure down to 25 mK in contrast with previous reports of superconductivity in this system [2,4,8,11]. Partial volume fraction superconductivity was confirmed by single-crystal ac susceptibility measurements illustrating the onset of superconductivity with small volume fractions at ambient pressure.

The relationship between pressure enhancement of superconductivity and the pressure driven transition to the $1T'$ phase from the T_d phase in both $MoTe_2$ and WTe_2 have been taken as evidence of a relationship between the structural transition and T_c enhancement [11,24] though this is not a settled matter in either material [4,11,25]. Via transport measurements, we are able to track a suppression of the T_d phase with pressure up to 0.82 GPa where T_S is suppressed to below 80 K as is shown in Fig. 2(a). Further increases in pressure show

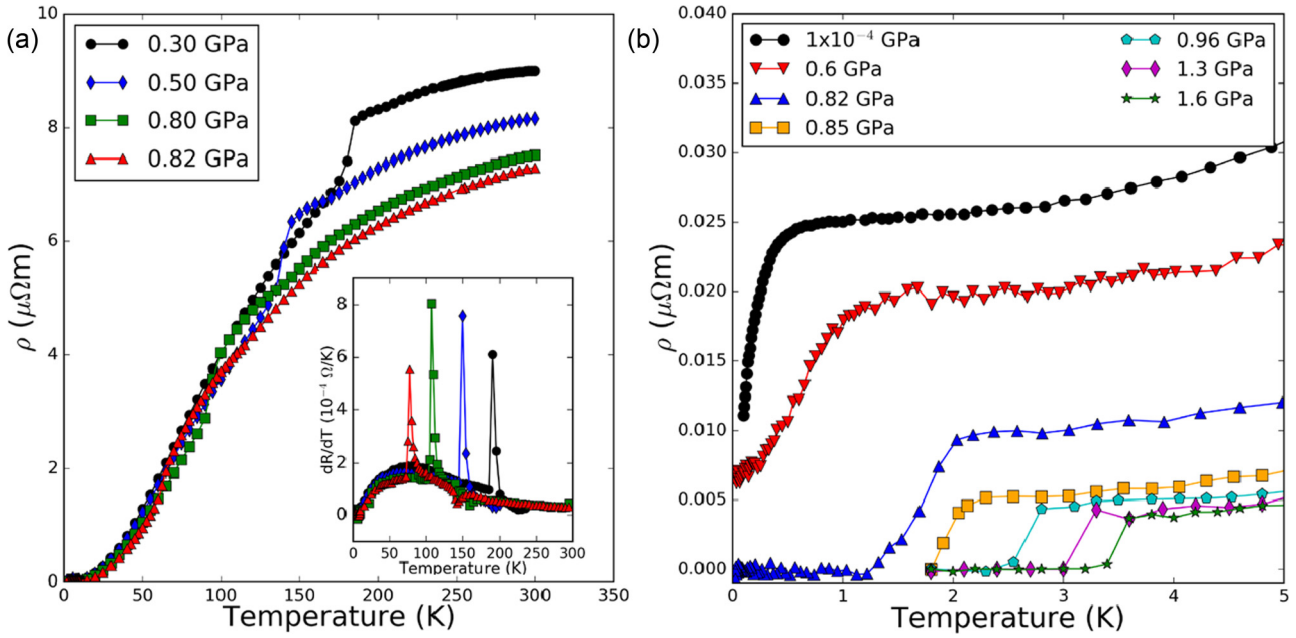

FIG. 2. Pressure dependence of transport measurements. (a) Pressure-dependent resistivity upon heating from 1.5 K. The kink in the resistivity indicates the position of the structural transition from the T_d phase to the $1T'$ phase. Inset shows differential resistance vs temperature clearly indicating T_S. We no longer see evidence of T_S above 0.82 GPa. (b) Pressure dependence of the superconducting T_c. We see a full resistive transition at 0.82 GPa and above.

no obvious kink in the resistivity nominally indicating that the noncentrosymmetric phase is unstable above 0.8 GPa, in contrast with the pressure phase diagram in [2] but consistent with the reports of [11] where the crystal symmetry change is assumed to enhance superconductivity. Furthermore, this 0.82-GPa pressure is also the point at which we observe the transition from a partially superconducting state to a full zero resistance state as is shown in Fig. 2(b).

Since the Weyl semimetal state can only exist with broken inversion symmetry, it is critical to directly probe the crystal structure of $MoTe_2$ in the superconducting state. Using elastic neutron scattering we have probed the $1T'$ to T_d structural transition as a function of pressure and temperature. To do this, we selected one set of reflections distinct between the T_d and $1T'$ phases in one crystal zone [the (201)-like reflections] and one set of reflections common to both phases [the (008) reflections] in the same zone and monitored those reflections through phase space. The convention for labeling (hkl) and crystallographic a, b, and c axes in the T_d and $1T'$ phases varies in the literature. Our convention for axis labeling and our reflection choice is explained in Supplemental Material Sec. II.A [21]. We will refer to the distinct reflections as the monoclinic (coming from the $1T'$ phase fraction) and orthorhombic (coming from the T_d phase fraction) reflections while referring to the common reflections as the (00l) reflections. Details of the various neutron-scattering measurements can be found in the experimental methods section [21].

At ambient pressure, we clearly see a first-order transition from the $1T'$ to the T_d phase upon cooling from room temperature while monitoring both the monoclinic and orthorhombic reflections, with a large coexistence region of more than 50 K. The mixed phase state is stable at these temperatures for time scales on the order of hours. Upon heating, we observe the return to the $1T'$ phase, though we observe a much larger coexistence region than is seen from transport. Our coexistence region is in line with previous Raman measurements and x-ray measurements which show a coexistence region of >50 K and the survival of a mode attributed to the T_d phase up to room temperature upon warming from the T_d phase [9,26]. This suggests that the transport signature, while clearly linked with the structural transition, is not a direct measure of the structural transition volume fraction. Instead, it may be indicating a percolationlike transition upon cooling (warming) with increasing (decreasing) T_d phase fraction. We also note that we see equal monoclinic twin populations both in the as grown samples and after cycling through the phase transition.

We next cooled our crystal down to 40 mK and confirmed that we saw no evidence of any reentrant monoclinic phase transition upon the onset of superconductivity. We also performed reciprocal space maps at a range of temperatures between 40 mK and 2 K, and see no evidence of any modulation of the intensity or shape of the orthorhombic reflections as the sample crosses the measured T_c for partial superconductivity. Despite our observation that our crystals do not reach a zero resistance state by 25 mK, if superconductivity were confined to monoclinic sample regions we would have expected to see a monoclinic phase fraction in the scattering.

Using a steel based gas pressure cell compatible with *in situ* neutron scattering as described in the Supplemental Material [21] and illustrated in Fig. 4(a), we monitored the same orthorhombic and monoclinic reflections as well as an (008) reflection over a pressure range from 0.02 to 1 GPa in a temperature range from 1.5 to 100 K. We initial cooled our sample to 63 K at 0.02 GPa and confirmed the expected T_d structure at this phase point [point i in Fig. 3(a)]. The 63-K temperature is chosen to maintain the He pressure medium in a liquid

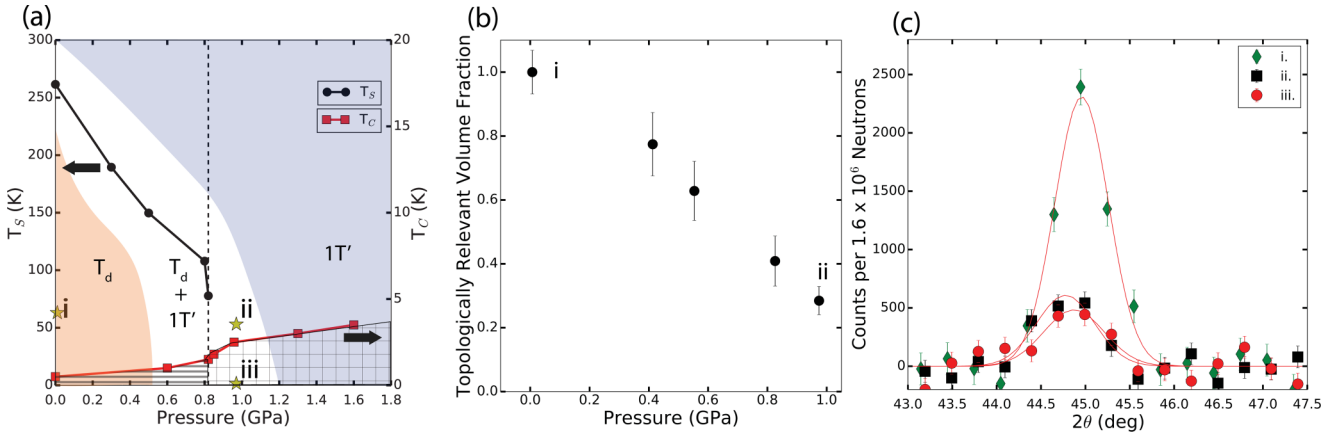

FIG. 3. Phase diagram and pressure-dependent neutron scattering for $MoTe_2$. (a) Transport generated phase diagram. Black circles represent $1T'$ to T_d structural transition temperature obtained from the dR/dT upon warming, red squares indicate onset of superconductivity from dR/dT. The dotted vertical line indicates the pressure at which we see concurrent loss of a structural resistance signature as well as the onset of a full zero resistance state. The yellow stars labeled with lower case roman numerals indicate the neutron measurements shown in (b) and (c). Horizontal cross hatching indicates partial superconductivity and grid cross hatching indicates full resistive transitions. Background color indicates structural phase (b). Phase fraction of the T_d phase as a function of applied pressure measured at 63 K. (c) Longitudinal scans along the orthorhombic peaks at points i–iii on the phase diagram in (a). Data are background subtracted.

or gaseous state over the entire pressure range up to 1 GPa. We then increased the pressure by supplying more He gas, and monitored the integrated intensity of longitudinal scans at the orthorhombic position. For these neutron measurements, all error bars and confidence intervals are given by standard deviations of the Poisson distribution.

Upon pressure increase, we immediately observe the start of the transition from the T_d to the $1T'$ phase, but surprisingly we see that a significant phase fraction ($30 \pm 5\%$) of the T_d phase survives up to our maximum pressure of 1 GPa, which is well above the nominal critical pressure from transport [11]. This pressure dependence of the T_d phase fraction is shown in Fig. 3(b), where the extracted phase fractions come from the ratio of the integrated intensity of the orthorhombic reflection [labeled as the $(201)_O$ reflection] at a given temperature and pressure to the intensity at 0.02 GPa and 63 K where the full volume fraction is T_d. We then cool from 63 K down to 1.5 K while maintaining 1 GPa and see no obvious change in the phase fraction of the T_d phase, which is shown in Fig. 3(c). It should be noted that due to differences in the structure factor between the monoclinic reflections and the orthorhombic reflection, as well as monoclinic twinning, the orthorhombic reflection is significantly more intense than the monoclinic reflections which limits our ability to detect small phase fractions of monoclinic phase above our background level. While we see a reduction in the orthorhombic peak intensity by 0.4 GPa, we do not see intensity at the monoclinic position until 0.6 GPa, and we attribute this is to our detection limits. By tracking the angular position of the monoclinic reflections we can track the β angle of the $1T'$ phase. We observe that β increases with pressure, consistent with both our DFT calculations (see Fig. S2 in the Supplemental Material) and with previously reported x-ray-diffraction measurements [2]. Importantly, as we observe intensity at the monoclinic peak positions, we see equal scattering intensity from both expected monoclinic twins in this zone indicating pressure homogeneity.

Our study has uncovered a complex interplay between the crystal structure of this system and the underlying electronic ground state. Below 0.8 GPa, our transport measurements indicate partial volume fraction superconductivity and show a strong anomaly related to the T_d to $1T'$ transition. The neutron-diffraction measurements show that the phase fraction of the low-pressure T_d phase also drops below 50% at 0.8 GPa. In contrast, previous ac susceptibility and muon spin-rotation (μSR) measurements indicate that within this pressure regime, full volume fraction superconductivity is achieved [4]. The large phase coexistence region in both pressure and temperature suggests that the T_d and $1T'$ phases are very close in energy. To address this interplay between pressure, structure, and superconductivity, we turn to first-principles calculations. In particular, we have calculated the pressure dependence of the stability of each phase, the reaction path between the measured structures, how the electron-phonon coupling changes between the T_d and $1T'$ phases, and whether both structures would be expected to support superconductivity. The details of these calculations are given in the supplemental material [21].

Our total-energy calculations indicate that (see Fig. S1 in the Supplemental Material) both phases are nearly degenerate and only separated by an energy barrier of 0.8 meV, in agreement with recent calculations [27] but in contrast to previous assumptions as to the origin of the large phase coexistence region between the T_d and $1T'$ phases [9,28]. The centrosymmetric phase $1T'$ always has a slightly lower volume than the noncentrosymmetric T_d phase with applied pressure and therefore at high pressure the enthalpy term prefers $1T'$ over T_d as shown in Fig. S3 of the Supplemental Material, justifying the pressure driven suppression of T_S. We have also calculated full phonon dispersion curves for both phases at different pressures up to 10 GPa and did not find any phonon softening to explain this structural transition (see Figs. S4 and S5) in contrast to [20]. Interestingly, the calculated free-energy when considering the full phonon dispersions at

ambient pressure also prefers the $1T'$ phase over the T_d phase at high temperatures as in the case of enthalpy. Hence, the observed phase transition is not soft-phonon driven but rather entropy driven [29].

To better explain this nonintuitive result we offer the following explanation. Qualitatively, when viewed orthogonal to the orthorhombic b-c plane [as is shown in Fig. 1(b)], the Mo-Te zigzag chains of atoms resemble opposed sawteeth across the van der Waals bonding. If one were to slide these two sheets past each other along the orthorhombic b direction they would observe a periodic potential as the sawteeth pass each other. As shown in Fig. S4(a) in the Supplemental Material, the interplane sliding mode along the long axis is very anharmonic and features two shallow minima. In the lowest energy minimum, the $MoTe_2$ planes (i.e., sawteeth points) are more on top of each other and the curvature of one minima is slightly larger than the other. This results in slightly higher phonon energies and also gives a larger c-axis lattice parameter. When one of the planes slides a small amount and enters the minima along b, the teeth of the sawlike planes interlock, causing a c-axis contraction but lowering the energy required for a transverse motion along a, giving lower phonon energies and higher entropy. At higher temperatures the system prefers this interlocked configuration where the c axis is shorter and intersliding phonons are lower in energy (here entropy dominates the free energy). This observation is consistent with the observed negative thermal expansion and the longer c axis of the lower temperature T_d phase. When we cool the system, entropy is less important and the system prefers to be at the minimum enthalpy configuration with the planes aligned on top of each other with a longer c axis and orthorhombic symmetry, but higher phonon energies.

We have also calculated the electron-phonon coupling (λ) for both structures. Despite the strong apparent correlation between structure and superconductivity, the calculated coupling in both phases is very similar, indicating that the main contribution to superconductivity comes from within a single layer $MoTe_2$ unit. Indeed we found very similar λ for both single layer $MoTe_2$ and bulklike $MoTe_2$ (see Supplemental Material Sec. D) [21]. For both bulklike phases and the single layer analog, we find that all phonon modes contribute to λ. This phase independent and apparent isotropic and energy independent contribution to λ suggests that there is some other contribution to superconductivity enhancement in $MoTe_2$ beyond the structural transition. The main difference between bulklike and single layer $MoTe_2$ is found to be the pressure dependence of the λ. For the case of bulk $MoTe_2$ we did not find significant pressure dependence (Fig. S12) while for a single layer, T_c is increased by an order of magnitude at 10 GPa pressure (Fig. S9) as experimentally observed [2].

The single layer nature of λ and the large structural phase coexistence region raises interesting questions about the nature and origins of superconductivity in $MoTe_2$. Previously reported ac susceptibility and μSR measurements demonstrated full volume superconductivity in this coexistence region, ruling out the possibility that superconductivity exists only in isolated regions of the sample where single layers may be structurally decoupled. The two-gap model needed to explain the temperature dependence of $\lambda_{\text{eff}}^{-2}$ (where λ_{eff} is the powder average effective magnetic penetration depth) in pressure-dependent μSR could indicate that there is a different superconductivity existing in the two phases [4]. The nature of the interfaces between noncentrosymmetric and centrosymmetric regions of the sample in the mixed phase may further lead to interesting physics and potentially different superconducting states between the two regions. These interfacial regions may even support different band topologies given the broken symmetry at the interfaces and the possibility for a Weyl semimetal in proximity to a superconductor. The apparent single layer nature of the pressure dependence of λ and the T_c enhancement observed empirically hints that some kind of single layer decoupling happens with hydrostatic pressure which is surprising. This could be due in part to the expected large number of stacking faults for a van der Waals bonded material, which have been demonstrated in $MoTe_2$ [30,31]. This is not to say that we are creating new stacking faults with pressure, but rather that pressure appears to make the system more quasi-two-dimensional (2D), which may be related to interactions and dynamics of pre-existing planar defects such as stacking faults. Furthermore, while the μSR study did not consider this, if this pressure enhanced superconductivity is quasi-2D and there is a spin-triplet component to the pairing (allowed by symmetry) this may be a further route to topological superconductivity [1,32,33]. Further characterization of the nature of superconductivity in the system that considers the actual populations of the two structural phases and their interfaces is needed to explore these possibilities.

Since we now do not expect that enhanced superconductivity must exist only in the centrosymmetric volume of a crystal, we can ask whether there is a way to independently control crystal symmetry and superconductivity. Given the small energy difference between the two phases, one might expect that experimentally achievable strains might also influence the preferred crystal structure. Indeed, our calculations shown in Fig. 4(d) show that uniaxial strain can stabilize either the T_d or $1T'$ phase depending on the crystallographic axis along which the strain is applied.

In an effort to take advantage of the calculated uniaxial strain dependence of the ground-state crystal structure, we have also performed structural measurements at the Oak Ridge National Laboratory High-Flux Isotope Reactor on the HB-3A four-circle diffractometer [34]. Here a clamp cell with a fluorinated pressure medium is used, similar to the cell described here [35]. This fluorinated pressure medium has also been demonstrated to be nonhydrostatic above 0.8 GPa, leading to a nonhydrostatic pressure environment in our cell [36]. Figures 4(a) and 4(b) illustrate the different cell geometries while Figs. 4(e) and 4(f) illustrate the difference stress environments within the cells. Here we have taken the standard notation where hydrostatic pressure corresponds to a stress tensor with equal and negative (compressive) diagonal components. With the clamping axis applying a larger uniaxial compressive stress along the monoclinic notation crystallographic b axis, this is equivalent to negative strain along b shown in Fig. 4(d). At a clamp loading corresponding to 1.5 GPa with this media, we observe clear evidence of nonhydrostatic pressure in the form of strain broadening and detwinning of the monoclinic phase. We also observe a complete change in the ground-state crystal structure. As shown in Fig. 4(g), at a nominal pressure of 1.5 GPa we lose all evidence of any monoclinic phase

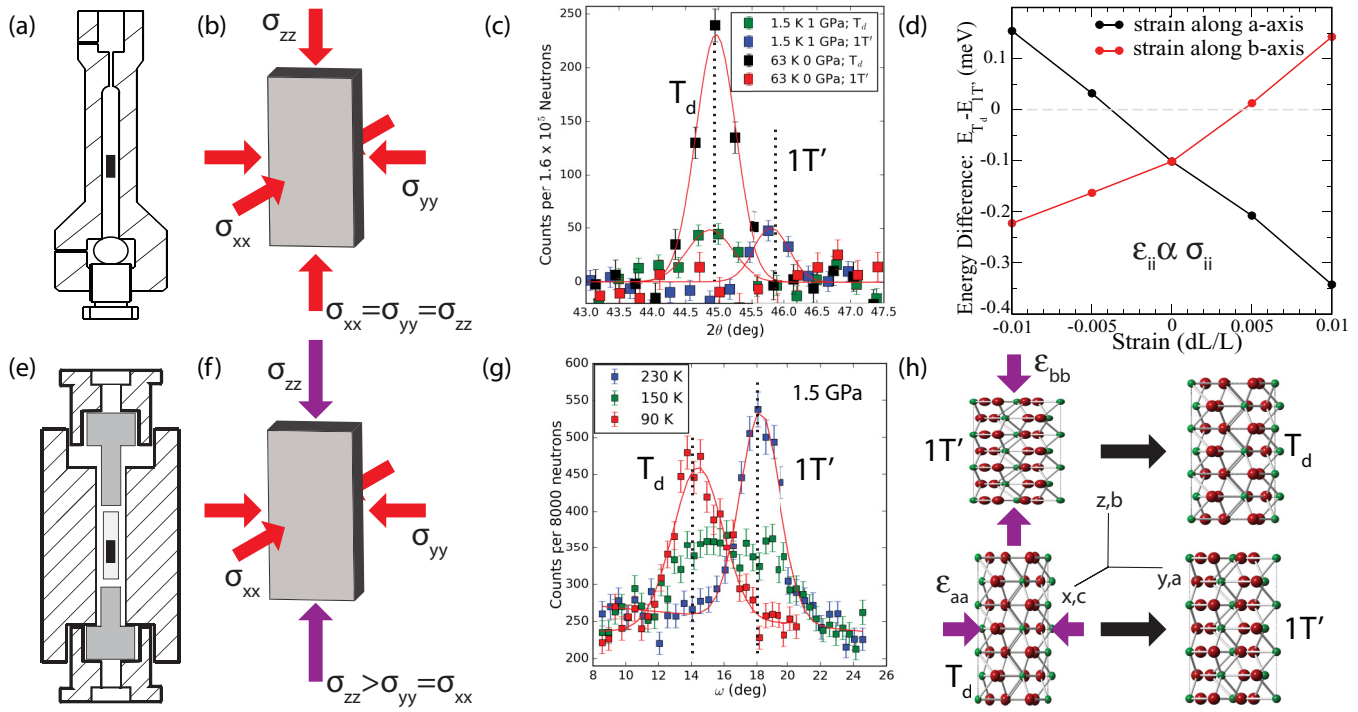

FIG. 4. Effect of strain field on crystal structure. (a) Schematic of of He gas cell used for hydrostatic pressure environment measurements. Gas is loaded externally into the cryostat (b). Stress environment for a platelike sample in the He cell assuming no shear. Stress is given as components of the stress tensor, with the convention that hydrostatic pressure is negative stress. (c) Longitudinal scans along $(021)_O$ (labeled T_d) and $(201)_M$ (labeled $1T'$) positions at ambient pressure (63 K) and at 1 GPa (1.5 K) for He cell. No peak is observed from the $1T'$ phase at ambient pressure. (d) DFT calculations of the energy difference between the T_d and $1T'$ phases as a function of strain along the a axis (black) and b axis (red) at ambient pressure. Compressive strain is negative by convention. (e) Diagram of the CuBe clamp cell used in the ORNL experiments. The sample is sealed in a capsule with fluoroinert pressure media and pistons uniaxially compress the capsule. (f) Stress environment for a platelike sample in the CuBe cell assuming no shear. Uniaxial loading and nonhydrostatic pressure transduction leads to increased stress component along clamping direction. (g) Rocking scans at $(021)_O$ and $(201)_M$ peak positions through the phase transition in the CuBe cell at 1.5 GPa. Below 90 K, we see no evidence of the $1T'$ phase (h). Unixaial strain along b drives phase from $1T'$ to T_d, uniaxial strain along the a axis drives a transition from the T_d phase to the $1T'$ phase. Axes illustrate the correspondence between monoclinic a, b, c and x, y, z in the stress diagrams.

below 90 K (measured down to 5 K). Upon warming the previously defined monoclinic reflection starts to show up at 100 K and the phase transition is completed by 230 K. This is in contrast to the observed coexistence from our He cell measurements shown in Figs. 3 and 4(c). Here we have clear evidence that the ground-state crystal structure can be controlled though careful design of the mechanical stress environment, but also that structural determination is critical for interpretation of other measurements. Other groups have also noted the empirical importance of uniaxial strain in this system for magnetotransport properties and for T_S at ambient pressure [37]. Our extracted single-crystal lattice parameters and the change in a/b ratio under pressure loading in this clamp cell (shown in Table S5 of the Supplemental Material) [21] are also consistent with a uniaxial stress geometry compared to the unloaded state.

The ability to stabilize the full volume fraction of the T_d phase with nonhydrostatic pressure offers a simple route to a monophase noncentrosymmetric superconductor. Given our calculations of λ in the two crystal structures, and given the full volume fraction superconductivity in polycrystalline samples from ac susceptibility [4], we should expect that the enhancement in superconductivity is independent of the ground-state crystal structure. One would expect no preferential phase selection in the polycrystalline system given the random orientation of grains with respect to possible nonhydrostatic pressure. Strain control of structure independent of superconductivity enhancement also explains the previous disagreements in pressure-temperature phase diagrams of T_S defined by transport [2,11]. We can think of $MoTe_2$ as offering a system where pressure tunes superconductivity through shifting the single layer electronic DOS and possibly decoupling the layers while in-plane stresses (strains) can select between the centrosymmetric and noncentrosymmetric phases. The huge stability window in both pressure and temperature of the mixed phase state offers a further unique opportunity for phase engineering in this system by tuning structural phase fractions.

Our results illustrate the possibility to independently control inversion symmetry breaking through structural manipulation in $MoTe_2$ as well as superconductivity in $MoTe_2$ using temperature, hydrostatic pressure, and the symmetry of nonhydrostatic components of pressure (uniaxial-like stress). This decoupling of the superconductivity from the structural transition explains previous disagreements between transport

and magnetic measurement generated T-P phase diagrams [2,4,11]. We have shown the coexistence of the T_d and $1T'$ phases at hydrostatic pressures and temperatures concurrent with full volume fraction superconductivity, which demonstrates that $MoTe_2$ can support topological superconductivity in certain regions of the sample, or in full sample volumes under nonhydrostatic pressure loading. The nature of this topological superconductivity can take multiple forms, whether through a proximity effect in the mixed phase region or through a full noncentrosymmetric bulk superconductivity in a Weyl semimetal. We anticipate that these results will help elucidate future interesting and useful transport properties in this material, and may offer a route towards a superconducting system with strain tunable Weyl Fermi arcs and nontrivial band topology.

We acknowledge useful discussions with C. M. Brown. Certain trade names and company products are identified in order to specify adequately the experimental procedure. In no case does such identification imply recommendation or endorsement by the National Institute of Standards and Technology, nor does it imply that the products are necessarily the best for the purpose. This research used resources at the High Flux Isotope Reactor, a DOE Office of Science User Facility operated by the Oak Ridge National Laboratory. Research at the University of Maryland was supported by AFOSR through Grant No. FA9550-14-1-0332 and the Gordon and Betty Moore Foundations EPiQS Initiative through Grant No. GBMF4419. Support for P.N. was provided by the Center for High Resolution Neutron Scattering, a partnership between the National Institute of Standards and Technology and the National Science Foundation under Agreement No. DMR-1508249.

C.H. and N.B. synthesized materials. C.H., W.R. II, Y.W., J.L., and H.C. performed neutron-scattering measurements. Bulk property measurements were performed by C.H., I-L.L., T.M., C.E., P.N., J.L., P.P., J.P. and N.B. L.H. and T.Y. performed DFT calculations. All authors contributed to the manuscript. The authors declare no competing financial interests.

[1] M. Sato and Y. Ando, Rep. Prog. Phys. **80**, 076501 (2017).
[2] Y. Qi, P. G. Naumov, M. N. Ali, C. R. Rajamathi, W. Schnelle, O. Barkalov, M. Hanfland, S.-C. Wu, C. Shekhar, Y. Sun *et al.*, Nat. Commun. **7**, 11038 (2016).
[3] X. Luo, F. Chen, J. Zhang, Q. Pei, G. Lin, W. Lu, Y. Han, C. Xi, W. Song, and Y. Sun, Appl. Phys. Lett. **109**, 102601 (2016).
[4] Z. Guguchia, F. Rohr, Z. Shermadini, A. Lee, S. Banerjee, A. Wieteska, C. Marianetti, B. Frandsen, H. Luetkens, Z. Gong *et al.*, Nat. Commun. **8**, 1082 (2017).
[5] L. Huang, T. M. McCormick, M. Ochi, Z. Zhao, M.-T. Suzuki, R. Arita, Y. Wu, D. Mou, H. Cao, J. Yan *et al.*, Nat. Mater. **15**, 1155 (2016).
[6] K. Deng, G. Wan, P. Deng, K. Zhang, S. Ding, E. Wang, M. Yan, H. Huang, H. Zhang, Z. Xu *et al.*, Nat. Phys. **12**, 1105 (2016).
[7] P. Deng, Z. Xu, K. Deng, K. Zhang, Y. Wu, H. Zhang, S. Zhou, and X. Chen, Phys. Rev. B **95**, 245110 (2017).
[8] D. Rhodes, R. Schönemann, N. Aryal, Q. Zhou, Q. Zhang, E. Kampert, Y.-C. Chiu, Y. Lai, Y. Shimura, G. McCandless *et al.*, Phys. Rev. B **96**, 165134 (2017).
[9] R. Clarke, E. Marseglia, and H. P. Hughes, Philos. Mag. B **38**, 121 (1978).
[10] B. E. Brown, Acta Crystallogr. **20**, 268 (1966).
[11] H. Takahashi, T. Akiba, K. Imura, T. Shiino, K. Deguchi, N. K. Sato, H. Sakai, M. S. Bahramy, and S. Ishiwata, Phys. Rev. B **95**, 100501(R) (2017).
[12] S. Cho, S. H. Kang, H. S. Yu, H. W. Kim, W. Ko, S. W. Hwang, W. H. Han, D.-H. Choe, Y. H. Jung, K. J. Chang *et al.*, 2D Mater. **4**, 021030 (2017).
[13] D. Rhodes, D. Chenet, B. Janicek, C. Nyby, Y. Lin, W. Jin, D. Edelberg, E. Mannebach, N. Finney, A. Antony *et al.*, Nano Lett. **17**, 1616 (2017).
[14] F. Chen, X. Luo, R. Xiao, W. Lu, B. Zhang, H. Yang, J. Li, Q. Pei, D. Shao, R. Zhang *et al.*, Appl. Phys. Lett. **108**, 162601 (2016).
[15] I. Belopolski, D. S. Sanchez, Y. Ishida, X. Pan, P. Yu, S.-Y. Xu, G. Chang, T.-R. Chang, H. Zheng, N. Alidoust *et al.*, Nat. Commun. **7**, 13643 (2016).
[16] Y.-Y. Lv, L. Cao, X. Li, B.-B. Zhang, K. Wang, B. Pang, L. Ma, D. Lin, S.-H. Yao, J. Zhou *et al.*, Sci. Rep. **7**, 44587 (2017).
[17] S. M. Oliver, R. Beams, S. Krylyuk, I. Kalish, A. K. Singh, A. Bruma, F. Tavazza, J. Joshi, I. R. Stone, S. J. Stranick *et al.*, 2D Mater. **4**, 045008 (2017).
[18] T. Kim, D. Puggioni, Y. Yuan, L. Xie, H. Zhou, N. Campbell, P. Ryan, Y. Choi, J.-W. Kim, J. Patzner *et al.*, Nature (London) **533**, 68 (2016).
[19] N. A. Benedek and C. J. Fennie, J. Phys. Chem. C **117**, 13339 (2013).
[20] K.-A. N. Duerloo, Y. Li, and E. J. Reed, Nat. Commun. **5**, 4214 (2014).
[21] See Supplemental Material at http://link.aps.org/supplemental/10.1103/PhysRevMaterials.2.074202 for details of experimental methods, crystallographic refinements, and calculations.
[22] T. Zandt, H. Dwelk, C. Janowitz, and R. Manzke, J. Alloys Compd. **442**, 216 (2007).
[23] H. Hughes and R. Friend, J. Phys. C **11**, L103 (1978).
[24] P. Lu, J.-S. Kim, J. Yang, H. Gao, J. Wu, D. Shao, B. Li, D. Zhou, J. Sun, D. Akinwande *et al.*, Phys. Rev. B **94**, 224512 (2016).
[25] Y. Zhou, X. Chen, N. Li, R. Zhang, X. Wang, C. An, Y. Zhou, X. Pan, F. Song, B. Wang *et al.*, AIP Adv. **6**, 075008 (2016).
[26] S.-Y. Chen, T. Goldstein, D. Venkataraman, A. Ramasubramaniam, and J. Yan, Nano Lett. **16**, 5852 (2016).
[27] H.-J. Kim, S.-H. Kang, I. Hamada, and Y.-W. Son, Phys. Rev. B **95**, 180101 (2017).
[28] W. Dawson and D. Bullett, J. Phys. C **20**, 6159 (1987).
[29] D. Frenkel, Physica A (Amsterdam) **263**, 26 (1999).
[30] X.-J. Yan, Y.-Y. Lv, L. Li, X. Li, S.-H. Yao, Y.-B. Chen, X.-P. Liu, H. Lu, M.-H. Lu, and Y.-F. Chen, npj Quantum Mater. **2**, 31 (2017).

[31] C. Manolikas, J. Van Landuyt, and S. Amelinckx, Phys. Status Solidi A **53**, 327 (1979).
[32] M. Sato and S. Fujimoto, Phys. Rev. B **79**, 094504 (2009).
[33] Y. Tanaka, T. Yokoyama, A. V. Balatsky, and N. Nagaosa, Phys. Rev. B **79**, 060505 (2009).
[34] B. C. Chakoumakos, H. Cao, F. Ye, A. D. Stoica, M. Popovici, M. Sundaram, W. Zhou, J. S. Hicks, G. W. Lynn, and R. A. Riedel, J. Appl. Crystallogr. **44**, 655 (2011).
[35] N. Aso, Y. Uwatoko, T. Fujiwara, G. Motoyama, S. Ban, Y. Homma, Y. Shiokawa, K. Hirota, and N. K. Sato, AIP Conf. Proc. **850**, 705 (2006).
[36] V. Sidorov and R. Sadykov, J. Phys.: Condens. Matter **17**, S3005 (2005).
[37] J. Yang, J. Colen, J. Liu, M. C. Nguyen, G.-w. Chern, and D. Louca, Sci. Adv. **3**, eaao4949 (2017).